



HAL
open science

Experimental velocity and temperature measurements for natural convection in a highly porous medium

Nicolò R Sgreva, Christel Métivier, Anthony Teixeira, Tien Dung Le,
Sébastien Leclerc

► **To cite this version:**

Nicolò R Sgreva, Christel Métivier, Anthony Teixeira, Tien Dung Le, Sébastien Leclerc. Experimental velocity and temperature measurements for natural convection in a highly porous medium. *International Journal of Thermal Sciences*, 2023, 205, pp.109257. 10.1016/j.ijthermalsci.2024.109257 . hal-04286807v1

HAL Id: hal-04286807

<https://hal.science/hal-04286807v1>

Submitted on 15 Nov 2023 (v1), last revised 18 Jul 2024 (v2)

HAL is a multi-disciplinary open access archive for the deposit and dissemination of scientific research documents, whether they are published or not. The documents may come from teaching and research institutions in France or abroad, or from public or private research centers.

L'archive ouverte pluridisciplinaire **HAL**, est destinée au dépôt et à la diffusion de documents scientifiques de niveau recherche, publiés ou non, émanant des établissements d'enseignement et de recherche français ou étrangers, des laboratoires publics ou privés.

Experimental velocity and temperature measurements for natural convection in a highly porous medium

Nicolò R. Sgreva*, Christel Métivier, Anthony Teixeira, Tien Dung Le,
Sébastien Leclerc

^aUniversité de Lorraine, CNRS, LEMTA, 54000, Nancy, France

Abstract

We present natural convection experiments at low-to-moderate porous media Rayleigh number Ra in a fluid-saturated structured plastic foam with porosity of 0.83 heated from below. This is motivated by the lack of detailed experiments on thermal convection in these systems, although they are of great interest for many engineering applications. Our experiments were carried out using Magnetic Resonance Imaging (MRI), which allowed us to obtain quantitative measurements of velocity vectors together with temperature fields in the bulk of the fluid-saturated sample. The results obtained are compared with those for classical porous media (e.g. packed beds of spheres) and with theoretical predictions.

For our system, we found the onset of convection at $Ra_c = 41.9$, with a critical wavenumber $\alpha_c \approx \pi$. For $Ra < Ra_c$, velocities always remain below the accuracy of the measurement and temperature fields remain homogeneous and linear in the vertical direction. For $Ra_c \leq Ra < 308$, the flow has a stable convective patterns in forms of axisymmetric, straight or deformed rolls. At about $Ra = 308$, the flow enters in a transitional regime in which the convective rolls begin to deform. At the highest Ra tested, the convective pattern takes the form of cross-rolls. The intensity of convection is estimated through the large-scale mean squared velocity U^2 . For $Ra > 70$, we obtain $U \sim Ra^{\frac{1}{2}}$.

The heat transfer is investigated by evaluating the Nusselt number from temperature fields. We found that the local Nu reflects the flow structure: higher values of local Nu correspond to cold down-welling regions,

*nicolo.sgreva@univ-lorraine.fr

and smaller Nu to warm up-welling regions. Finally, we found that the averaged Nusselt number for the whole system increases linearly with Ra with a slope equal to 2.

Keywords: Solid foam, Natural convection, Magnetic Resonance Imaging (MRI), Porous media

1 Introduction

Thermal convection in porous media is a key aspect in many natural phenomena and engineering applications. The former include convective flow of magma in partially crystallized reservoir (Tait and Jaupart, 1992) and groundwater circulation (Diersch and Kolditz, 2002). While in industry, examples include insulation systems (Rees and Lage, 1996) and thermal energy storage systems (Agyenim et al., 2010). In the case of thermal energy storage systems, porous media can be combined with phase change materials to form composite systems in which heat is stored and released more efficiently. In this case, the most commonly used macroscopic supports are highly porous open-cell solid foams (Zhang et al., 2021). In fact, these composite systems can store a large amount of phase change material, have a large surface area to volume ratio, and improve the melting rate (Yao et al., 2018). These are made of different materials and typically have a randomly organized solid structure or are characterized by unit cells with a specific geometry (Qureshi et al., 2021). When these composite systems are subjected to a temperature gradient, heat is transferred by conduction and, depending on the system and boundary conditions, by convection. The competition between the two heat transfer mechanisms depends on the thermal properties of the materials employed, the ability of the fluid to flow between the pores, and the heating position (Gasow et al., 2022; Krishna et al., 2009).

In these cases, a configuration of thermal convection of interest is the porous medium analogue of the Rayleigh-Bénard convection, where a fluid-saturated porous medium is uniformly heated from below and cooled from above. In this case, the fluid flow regime is characterized by the porous medium Rayleigh number (Ra), defined as

$$Ra = Ra_f \times Da = \frac{\rho g \beta \Delta T H K}{\eta \kappa_{\text{eff}}}, \quad (1)$$

where Ra_f is the Rayleigh number for a non-porous fluid layer and $Da =$

28 K/H^2 is the Darcy number. In eq. (1), ρ indicates the density of the fluid, β
 29 its thermal expansion coefficient, η its viscosity; g is the acceleration due to
 30 gravity, H the thickness of the layer, ΔT the temperature difference across
 31 this thickness, K the permeability and κ_{eff} the effective thermal diffusivity
 32 of the system. From linear stability analysis, when Ra remains smaller than
 33 a critical value, i.e. $Ra < Ra_c$, the conductive regime remains stable, the
 34 temperature field is uniform and there is no flow (Lapwood, 1948; Horton
 35 and Rogers Jr, 1945). The critical value $Ra_c = 4\pi^2$ has been verified several
 36 time for different types of porous media and fluids (Nield and Bejan, 2017).
 37 Large-scale convection in form of cellular motion develops for $Ra > Ra_c$. For
 38 sufficiently small Ra ($Ra_c < Ra < 300$), numerical computations based on
 39 spectral method show that convection is stable and the convective pattern
 40 is characterized by various types of rolls: counter-rotating rolls, superposi-
 41 tion of counter-rotating rolls, and polyhedral cells (Caltagirone and Fabrie,
 42 1989). For larger Ra , the flow is perturbed and becomes less stable due to
 43 boundary-layer instabilities. The background cellular structure is preserved
 44 until the transition to high- Ra convection from which rolls are completely
 45 destabilized (Hewitt, 2020). Most experimental work at low-moderate Ra ,
 46 however, reports irregular polygons from the onset (Howle, 2002), and only
 47 a few experiments have succeeded in reproducing the predicted pattern evo-
 48 lution (e.g. Howle et al., 1997; Shattuck et al., 1997). The latter were per-
 49 formed with classical porous media (packed beds of beads or ordered grids)
 50 with relatively low porosity (~ 0.4 - 0.5).

51 The case of natural convection in highly porous systems was studied by
 52 Kathare et al. (2008) and Davidson et al. (2009) who used water-saturated
 53 metal and carbon foams. They performed heat transfer measurements and
 54 found that the Nusselt number increases with increasing Ra less than re-
 55 ported for beads. Moreover, for relatively small Ra , the heat transfer en-
 56 hancement provided by the metal foam occurs mainly by conduction. Shiina
 57 and Hishida (2010) studied the effects that an anisotropic effective thermal
 58 diffusivity has on the onset of convection in a highly porous system formed
 59 by thin wires deployed between the two horizontal plates. In this case, the
 60 critical Rayleigh number was found to depend on both Da and the degree of
 61 thermal diffusion anisotropy.

62 Despite the importance of natural convection, in-depth experiments in
 63 porous media, and especially in highly porous systems, remain rare because
 64 they are particularly difficult to carry out. In most of them, an idealized
 65 granular medium (e.g., packed beds of spheres) or a Hele-Shaw cell is used to

66 model the porous medium (Hewitt, 2020). Although the latter allows optical
67 access, it cannot be used to analyze three-dimensional flows and materials
68 with more complex geometries (e.g., with different pore sizes, different pore
69 paths, etc.). On the other hand, the use of a standard porous matrix limits
70 the use of classical optical devices for flow visualization and generally forces
71 the use of invasive measurement techniques. For this reason, most exper-
72 imental work focuses on measurements of heat transfer within the system,
73 without examining the velocity and temperature fields of the convective fluid.

74 In recent years, a few experimental techniques have been proposed and
75 tested to resolve fluid flow in the bulk of a fluid-saturated porous material.

76 Combining heat transfer measurements and optical measurement tech-
77 niques, Ataei-Dadavi et al. (2019) studied natural convection in a porous
78 medium consisting of a bed of packed coarse spheres. Using fluids and porous
79 media with the same refracting index, they have been able to visualize both
80 velocity and temperature fields. They found two regimes of heat transfer: a
81 reduced regime at low Ra , due to the poor penetration of fluid flow through
82 the pores, and a second regime for higher Ra , in which heat transfer is en-
83 hanced through the porous medium due to the increased rate of flow penetra-
84 tion across the pores. However, this experimental approach limits the choice
85 of system, which must consist of transparent materials with a refracting index
86 similar to that of the liquid within it.

87 A different way to visualize flow through an opaque media is by using
88 Magnetic Resonance Imaging (MRI). In this respect, the first attempt was
89 done by Shattuck et al. (1995) and Shattuck et al. (1997), who used MRI to
90 measure velocity field and investigate convective patterns at various Ra in
91 a packed beds of spheres heated from below and cooled from above. They
92 found that in disordered media, localized convection begins at $Ra < Ra_c$
93 due to packing defects that lead to locally larger porosity. In ordered media
94 convection is characterized by convective rolls up to $5Ra_c$, but with smaller
95 wavelength than those predicted by theory. Also, for slightly larger Ra (up
96 to $8Ra_c$), they obtained a time-dependent state where upward flow regions
97 move randomly in a larger area of downward flow.

98 Although MRI can provide quantitative information on velocity and tem-
99 perature, after this first attempt only a few other authors have used this
100 technique to investigate convection in porous media. Weber and Kimmich
101 (2002) studied thermal convection in a random-site percolation network using
102 MRI for velocity and temperature mapping. Skuntz et al. (2018) and Skuntz
103 et al. (2021) analyzed the fluid flow and the melting front of a non-isothermal

104 packed bed of beads containing a phase change material. And Wang et al.
105 (2021) carried out experiments of buoyancy-driven convection in an hetero-
106 geneous pack of beads. In all these cases, the porous medium was designed
107 by stacking beads together, strongly limiting the maximum possible porosity
108 of the system (the typical porosity for beds of packed spheres is $\phi \sim 0.40$).

109 In this work we aim to study natural convection at low-to-moderate Ra
110 an open-cell solid foam with high porosity ($\phi > 0.80$). This is motivated by
111 the lack of detailed experiments on convection in structured solid foam, al-
112 though it is an extremely important topic for many engineering applications.
113 For this purpose, we carried out experiments using a Kelvin-cell foam as a
114 solid matrix filled with Newtonian liquids. The fluid-saturated foam is then
115 placed in a cylindrical cavity heated from below and cooled from above. We
116 use MRI to measure velocity vectors and temperature fields of the convective
117 fluid within the solid matrix. The materials used during the experiments and
118 their properties are discussed in sect. 2. In sect. 3 we detail the experimental
119 setup and we describe the protocols used for MRI measurements. Results for
120 the onset of convection, evolution of convection patterns, intensity of con-
121 vection and heat transport are reported in sect. 4. Here we also compare
122 the results obtained for the convection in solid foam with those reported in
123 literature for more classical and idealized porous media. The paper ends with
124 a summary and some concluding remarks in sect. 5.

125 **2. Materials and their properties**

126 *2.1. Fluids*

127 Two different Newtonian fluids were used during our experiments: glyce-
128 rol (85 wt% solution in water) and a paraffin (hexadecane).

129 The glycerol aqueous solution was prepared by adding demineralized wa-
130 ter to pure glycerol, with the latter used as received from the supplier (Fisher
131 Chemical, with a stated purity of 99 %). Its thermophysical properties at a
132 temperature of 25 °C are summarized in Table 1. The density ρ was measured
133 at ambient atmospheric pressure with a DMA 5000M Anton-Paar densime-
134 ter. The coefficient of thermal expansion β was evaluated from the density
135 measurements from $\beta(T_0) = -\rho^{-1}(T_0)(\partial\rho/\partial T)_{T_0}$, with T being the tempera-
136 ture and T_0 the reference temperature. The viscosity η was measured with a
137 stress-controlled AR-G2 rheometer (TA instrument) in rotational mode. The
138 measured values (Table 1) are in good agreement with those expected for the
139 same glycerol aqueous solution, see for instance Takamura et al. (2012).

Table 1: Material properties at $T = 25$ °C. ρ is the density, η the dynamic viscosity, λ the thermal conductivity and β the coefficient of thermal expansion. The standard uncertainties u_a for the measured properties are $u_a(\rho) = 0.01$ kg m⁻³, $u_a(\eta) = 5 \times 10^{-4}$ Pa.s, and $u_a(\beta) = 2.7 \times 10^{-6}$ °C⁻¹ with $u_a(T) = 0.01$ °C. The other material properties are from: ^[a]: Sgreva et al. (2023) and ^[b]: Sgreva et al. (2022).

Material	ρ (kg m ⁻³)	η (Pa.s)	λ (W m ⁻¹ K ⁻¹)	β (°C ⁻¹)
85 wt% glycerol	1215.92	0.0818	0.310 ^[a]	5.066×10^{-4}
Hexadecane	770 ^[b]	0.003 ^[b]	0.150 ^[b]	8.861×10^{-4} ^[b]
Plastic foam	1192 ^[a]	-	0.192 ^[a]	-

140 Hexadecane was supplied by Sigma-Aldrich and labeled as 99% pure.
 141 Samples of hexadecane were used as received, i.e. without any further pu-
 142 rification or removing impurities. A complete characterization in terms of
 143 thermophysical properties of this paraffin is given in Sgreva et al. (2022)
 144 and Klochko et al. (2022). The values we report in Table 1 are those given
 145 in these last references. The crystallization temperature of hexadecane is
 146 $T_s = 17.3$ °C (Sgreva et al., 2022). In all experiments with this fluid, the
 147 applied temperatures were always larger than T_s and the material was always
 148 in liquid phase.

149 2.2. The porous medium

150 A structured solid foam with open cells was used as a porous medium.
 151 The foam sample was 3D-printed using a light-sensitive photopolymer resin
 152 (Monocure 3D Rapid, Monocure Pty Ltd., Australia). The 3D model (Fig.
 153 1) is made by assembling individual Kelvin-type cells to form a cylindrical
 154 disk of diameter $D = 114$ mm and height $H = 26$ mm. The Kelvin-type unit
 155 cell has a diameter (i.e. the distance between two opposing square faces)
 156 of 6.5 mm, and cylindrical struts with an approximate diameter of 1.2 mm.
 157 The printed foam sample consists then of four vertically stacked cells.

158 A sample's porosity of $\phi = 0.83 \pm 0.02$ was estimated from both magnetic
 159 resonance images and via water (volume) absorption. Density and other
 160 relevant thermal properties of the solid plastic are reported in Sgreva et al.
 161 (2023). According to it, at a temperature of 25 °C, the density of the solid
 162 plastic is 1192 kg m⁻³, the thermal conductivity is 0.192 W m⁻¹K⁻¹ (Table
 163 1), and the heat capacity is 1.56 kJ kg⁻¹K⁻¹.

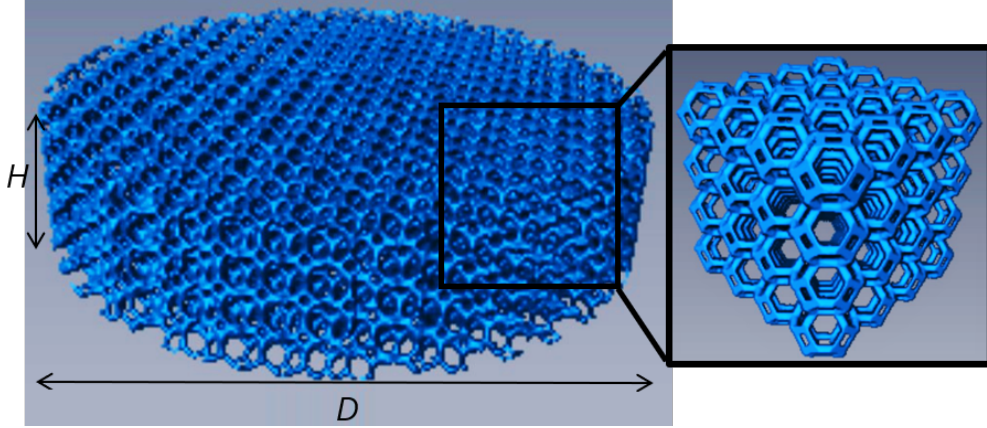


Figure 1: 3D model used to print the foam sample. The foam disk has a diameter $D = 114$ mm and a height of $H = 26$ mm.

164 *2.3. Effective properties of the system*

165 In order to evaluate Ra from eq.(1), two properties of the volume sample
 166 are required: the effective thermal diffusivity κ_{eff} of the whole system (i.e.
 167 solid matrix and fluid together) and the permeability K of the porous matrix.

168 Although κ_{eff} depends on the thermal diffusivity of the solid matrix and
 169 the saturating fluid, expressing it as a weighted arithmetic average of the
 170 two contributions is usually not recommended, especially when the thermal
 171 conductivity of the different phases is very different from each other (Smith
 172 et al., 2013).

173 In our case, the effective thermal diffusivity of the system consisting of the
 174 85% aqueous glycerol solution and the solid foam was previously measured
 175 experimentally in Sgreva et al. (2023) and the resulting effective thermal
 176 diffusivity is $\kappa_{\text{eff}} = 9.83 \times 10^{-8} \text{ m}^2\text{s}^{-1}$ (Table 2). For the case where the satu-
 177 rating fluid is hexadecane a direct measurement is not available. However, as
 178 shown by Smith et al. (2013) and Sgreva et al. (2023), an estimation of κ_{eff}
 179 can be obtained through the Hashin-Shtrikman model (Hashin and Shtrik-
 180 man, 1962). The latter is based on the volume fraction of the different system
 181 components and their thermal conductivities. By using this equivalent model
 182 and the weighted average of the volumetric heat capacity of solid and liquid
 183 phase, the effective thermal diffusivity for the hexadecane-saturated foam is
 184 $\kappa_{\text{eff}} = 8.97 \times 10^{-8} \text{ m}^2\text{s}^{-1}$ (Table 2).

185 Because of the different viscosities of the saturating fluids and the different

Table 2: Effective thermal properties and permeability of the two systems used for the experiments.

Property	Foam + 85wt% glycerol	Foam + hexadecane
Thermal diffusivity (κ_{eff})	$9.83 \times 10^{-8} \text{ m}^2\text{s}^{-1}$	$8.97 \times 10^{-8} \text{ m}^2\text{s}^{-1}$
Volumetric heat capacity (ρc_P)	$2.95 \times 10^6 \text{ J m}^{-3}\text{K}^{-1}$	$1.75 \times 10^6 \text{ J m}^{-3}\text{K}^{-1}$
Permeability (K)	$2.83 \times 10^{-7} \text{ m}^2$	$2.83 \times 10^{-7} \text{ m}^2$

186 effective thermal diffusivities, the two systems used for the experiments result
 187 in two different Prandtl numbers, $Pr = \eta/(\rho\kappa_{\text{eff}})$. At around $T = 25 \text{ }^\circ\text{C}$,
 188 we obtain a moderate Prandtl number for the hexadecane-saturated foam
 189 ($Pr = 43.5$) and a larger Prandtl number for the glycerol-saturated foam
 190 ($Pr = 688.1$).

191 For an ideal porous medium made by packed beds of spheres, the perme-
 192 ability K is defined by the Kozeny–Carman equation. In the case of highly
 193 porous systems, such as solid foams, the latter model cannot be used and
 194 the permeability must be evaluated by experiments or numerical simulations
 195 of pressure drop (Yang et al., 2021). These experiments have some com-
 196 plexities, such as the difficulty in establishing the flow regime (Dukhan and
 197 Minjeur, 2011) and the proper definition of the morphological parameters
 198 used as characteristic length scale (Kumar and Topin, 2017), that can lead
 199 to incorrect estimates of flow characteristics. In our case, the permeability
 200 was numerically estimated by solving the Stokes flow on the digital 3D geom-
 201 etry used to print the foam sample. A cubic portion of dimension $26 \times 26 \times 26$
 202 mm with a voxel size of 0.1 mm^3 was cropped from the initial 3D image
 203 of $114 \times 114 \times 26$ mm (Fig. 1), and was then segmented and meshed by us-
 204 ing AVIZO software. COMSOL Multiphysics software based on the finite
 205 element method was used to solve the Stokes equations with the Dirichlet
 206 boundary condition for the pressure at two opposite faces of the domain in
 207 order to obtain the velocity field. The permeability in the flow direction (the
 208 direction perpendicular to the faces where the pressure is imposed) can be
 209 calculated from the Darcy’s law by averaging the velocity field in this direc-
 210 tion. Since the sample is isotropic, simulation in only one direction is needed
 211 to estimate the permeability value. The value of permeability obtained in
 212 this way is $K = 2.83 \times 10^{-7} \text{ m}^2$ (Table 2), leading to $Da = 4.2 \times 10^{-4}$. In the
 213 same way, we evaluated the tortuosity of the digital porous medium from
 214 the effective diffusion coefficient. This led to a value for the tortuosity of the

215 foam of 1.3.

216 3. Setup and methods

217 3.1. Experimental setup and protocols

218 To investigate natural convection in the fluid-saturated solid foam, we
219 used an experimental setup similar to that used in Noel et al. (2022) and
220 Leclerc and Métivier (2018). The setup consists of a cylindrical PMMA
221 cavity containing the saturated foam (Fig. 2a). The cavity has the same
222 dimension as the foam disk, that is, an inner diameter of $D = 114$ mm and
223 a height of $H = 26$ mm (aspect ratio $\Gamma = D/H = 4.4$). The solid foam was
224 inserted into the cavity by ensuring good contacts with the internal wall of
225 the PMMA cavity (i.e. no significant gap between foam and cavity wall), and
226 afterward it was carefully filled with the fluid. Air bubbles were removed by
227 manually shaking the device with the help of two small tubes inserted later-
228 ally into the cavity through the PMMA ring. The absence of air bubbles was
229 also verified during the experiments directly from magnetic resonance im-
230 ages. Temperatures above (T_{up}) and below (T_{dw}) the cavity were imposed by
231 water flows from temperature-controlled water baths. Each temperature was
232 measured with two K-type thermocouples (uncertainty of 1%), one placed at
233 the inlet of the water flow and one at the outlet. In this way, T_{up} and T_{dw}
234 indicate the average of the measured inlet and outlet temperatures above and
235 below the cavity, respectively. Good thermal contacts between water flows
236 and the sample were provided by two 3.1-mm-thick sapphire plates with a
237 thermal conductivity of around $35 - 40 \text{ W m}^{-1}\text{K}^{-1}$. The small thickness and
238 the large thermal conductivity of these plates lead to negligible temperature
239 variations within them. The device was also insulated with a thick layer of
240 insulating foam added to the outside of the side wall.

241 We applied the following protocol for the experiments. The fluid-saturated
242 foam was initially kept under isothermal conditions ($T_{up} = T_{dw} = T_0$, with
243 T_0 being an initial temperature) for a minimum of 5 hours. When thermal
244 equilibrium was reached, to obtain convection a temperature difference of
245 $\Delta T = T_{dw} - T_{up} > 0$ was imposed between top and bottom surfaces. ΔT
246 was afterwards varied by imposing further increments or decrements. The
247 waiting time between each change of ΔT varied from a minimum of 5 hours
248 to more than 12 hours. Temperature and velocity fields within the sample
249 were measured at the steady-state. During the entire procedure, the mean
250 temperature $T_m = (T_{dw} + T_{up})/2$ was always kept constant at around $24 \text{ }^\circ\text{C}$.

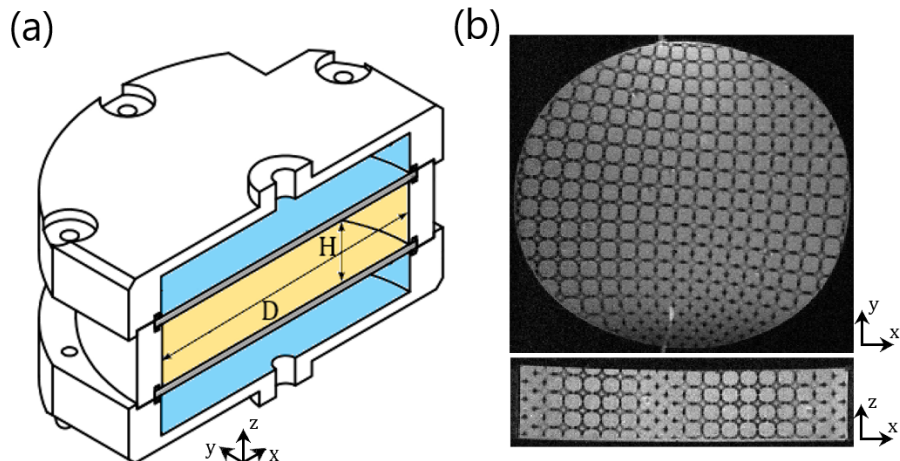


Figure 2: (a) Scheme of half of the experimental setup. We indicate in yellow the cavity containing the sample. (b) Proton density image of a 2 mm horizontal slice (along the xy -plane) and vertical slice (along the xz -plane) of the fluid-saturated solid foam. The horizontal image is taken at half the height of the cavity (i.e. $H/2$, with $H = 0$ on the lower plate of the cavity), while the vertical image crosses the cavity along its central axis.

251 *3.2. Magnetic Resonance Imaging (MRI)*

252 MRI experiments were performed with a Bruker Avance Biospec 24/40
 253 spectrometer in a temperature-controlled room at $T_{\text{room}} = 24$ °C. The spec-
 254 trometer was equipped with a 200-mm wide gradient coil delivering a 200
 255 mT/m maximum gradient strength and a 160-mm wide quadrature resonator.
 256 The horizontal magnetic field and the proton resonance frequency were 2.34
 257 T and 100.3 MHz, respectively.

258 MRI images were acquired with a slice thickness of 2 mm in a field of
 259 view of 120×120 mm. Horizontal images were acquired in the xy -plane at
 260 mid-height of the cavity (i.e., at $H/2$), while vertical images were acquired in
 261 the xz and yz planes along the center axis of the cavity (Fig. 2b). Because
 262 of the relatively large extent of the setup relative to the resonator and the
 263 gradient coil, the accuracy of MRI measurements is highest in the central
 264 part of the images, while the boundaries of the images are characterized by
 265 slight distortions of the acquired signal (Leclerc and Métivier, 2018).

266 MRI was used for three types of measurements: to identify (i) different
 267 phases (i.e., the solid foam and the fluid in it), and to obtain (ii) temperature
 268 fields and (iii) velocity vectors in the fluid. To do so, the following MRI
 269 protocols were used.

270 (i) Identification and reconstruction of the solid foam geometry were car-
 271 ried out by acquisition of fast proton density maps using Rapid Acquisition
 272 with Relaxation Enhancement (RARE) experiments (Hennig et al., 1986).
 273 The identification of the solid structure is possible because of its very fast
 274 transverse relaxation time, which leads to absence of signal. Images were
 275 acquired with resolutions of 128×128 and 256×256 pixels (for a minimum
 276 pixel length of 0.47 mm). We used an echo time (t_E) of 14 ms, a repetition
 277 time (t_R) of 1000 ms, and a RARE factor of 8.

278 (ii) Magnetic Resonance Thermometry (MRT) was used to obtain temper-
 279 ature fields of the saturating fluid (Leclerc and Métivier, 2018). Temperature
 280 can be achieved when the transverse component of the magnetic relaxation
 281 time (T_2^{NMR}), i.e. the time required for the magnetization vector to return to
 282 its equilibrium state after being subjected to a perturbation, shows a mono-
 283 tonic dependence with temperature. In our case, this occurred only for the
 284 aqueous solution of glycerol, but not for hexadecane. For hexadecane, the
 285 relaxation time did not show a strong dependence on temperature, thus not
 286 allowing MRT to be used. For 85 wt% glycerol, T_2^{NMR} images were obtained
 287 by Multi-Slice Multi-Echo (MSME) sequences (Leclerc and Métivier, 2018).
 288 We used 12 consecutive echoes, $t_E = 20$ ms and $t_R = 1000$ ms. Images had
 289 a resolution of 128×128 pixels and were averaged 16 times. The final tem-
 290 perature fields were obtained after a calibration performed under isothermal
 291 conditions, in which the correlation between temperature and T_2^{NMR} was es-
 292 tablished (Fig. 3). The global uncertainty for MRT measurement evaluated
 293 during the calibration process is $u(T) = 0.96$ °C, with a standard uncertainty
 294 $u_a(T) = 0.95$ °C and an uncertainty on T_{up} and T_{dw} due to thermocouple
 295 measurements of 0.10 °C (Leclerc and Métivier, 2018).

296 (iii) Magnetic Resonance Velocimetry (MRV) was used to obtain velocity
 297 fields of the fluid within the porous medium. Velocity images were obtained
 298 using similar protocols and the same pulse sequence of that of Noel et al.
 299 (2022). We used spin-echo imaging sequences together with flow encoding
 300 gradient pulses to acquire images with a 128×128 pixel resolution. The gra-
 301 dient pulse duration was $\delta = 4$ ms, the gradient separation time $\Delta_G = 12$
 302 ms, $t_E = 28$ ms, and $t_R = 800$ ms or $t_R = 1000$ ms for experiments with glyc-
 303 erol or hexadecane, respectively. We used a minimum flow encoding gradient
 304 pulse intensity of $G_{\min} = 0$ mT/m. Because of the different velocities reached
 305 during convection in the two fluids, we used a maximum gradient intensity of
 306 $G_{\max} = 180$ mT m⁻¹ for the 85 wt% glycerol solution and $G_{\max} = 175$ mT m⁻¹
 307 for hexadecane. The velocity field in the direction of the application of the

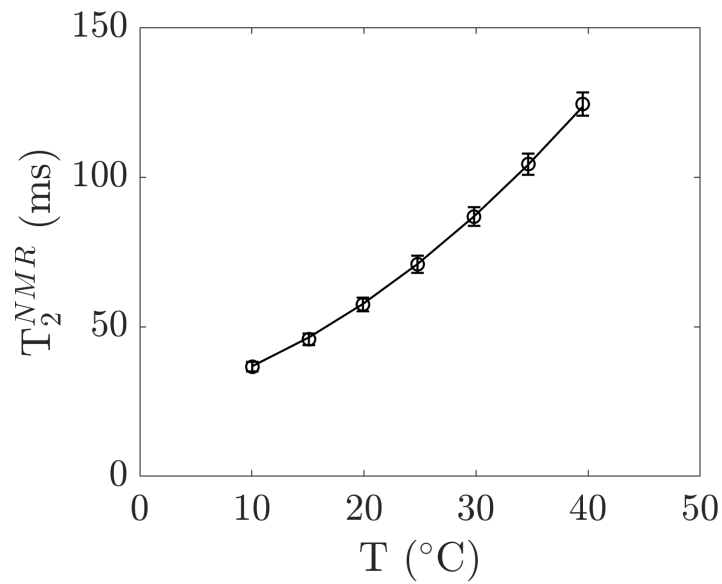


Figure 3: MRT calibration for the foam saturated with the 85 wt% glycerol solution at isothermal conditions ($T = T_{up} = T_{dw}$). The figure displays the transverse components of relaxation time T_2^{NMR} as a function of imposed temperature T . Data points are fitted by the second order polynomial fit $T_2^{\text{NMR}} = 24.161 + 0.835T + 0.043T^2$.

308 gradient is obtained from the difference between the image acquired with
 309 G_{\max} and that with G_{\min} . Following this protocol, the velocity resolution is
 310 $5 \times 10^{-5} \text{ m s}^{-1}$. The global uncertainty for MRV measurements is then esti-
 311 mated from reference images under isothermal conditions in $u(v) = 6.8 \times 10^{-5}$
 312 m s^{-1} , with v being the measured velocity.

313 Differently from MRT where the relaxation time does not depend on
 314 the amount of fluid in each voxel, Partial Volume Effect (PVE) arises during
 315 MRV if the solid matrix and the saturating fluid are both present in the same
 316 voxel. In this case, the voxel signal depends also on the fluid volume fraction
 317 in it. In our case, the latter is estimated from normalized RARE images. The
 318 normalization is done between the RARE maximum signal, corresponding
 319 to a voxel containing only fluid, and the minimum signal corresponding to
 320 a voxel of only solid material. The final velocity image, $I_{\text{velocity}}^{\text{final}}$, is then
 321 obtained as follows:

$$I_{\text{velocity}}^{\text{final}} = (I_{\text{velocity}}^{\text{raw}} - I_{\text{velocity}}^{\text{ref}}) \times I_{\text{RARE}}^*, \quad (2)$$

322 where $I_{\text{velocity}}^{\text{raw}}$ is the velocity image originally acquired, $I_{\text{velocity}}^{\text{ref}}$ is a reference
 323 velocity image obtained without fluid motion ($\Delta T \leq 0$), and I_{RARE}^* is the
 324 normalized RARE image for the fluid volume fraction.

325 4. Experimental results

326 4.1. Velocity and temperature measurements and onset of convection

327 Figure 4 shows an example of vertical velocity (Fig. 4a) and temperature
 328 field (Fig. 4b) within the sample for steady convection at $Ra = 123$ obtained
 329 with MRV and MRT, respectively. Here the fluid saturating the solid foam
 330 is the glycerol solution and the imposed temperature difference is $\Delta T =$
 331 $22.3 \text{ }^\circ\text{C}$. Images were acquired 5 hours after setting the temperatures. In
 332 the vertical scan of Fig. 4b, we also report the contour of three isotherms
 333 ($20 \text{ }^\circ\text{C}$, $25 \text{ }^\circ\text{C}$ and $30 \text{ }^\circ\text{C}$) to better distinguish temperature distribution.
 334 Figure 4 highlights the good agreement between velocity and temperature
 335 fields in both planar and vertical scans. In fact, the upward flow (positive
 336 vertical velocity) corresponds well to the warmer regions of the fluid, while
 337 the downward part of the convective pattern matches the cooler areas.

338 The convective pattern obtained in Fig. 4 is characterized by convection
 339 rolls. This is similar to results of Shattuck et al. (1997) and Howle et al.
 340 (1997) for ordered porous media but with a lower porosity ($\phi \leq 0.5$) than in

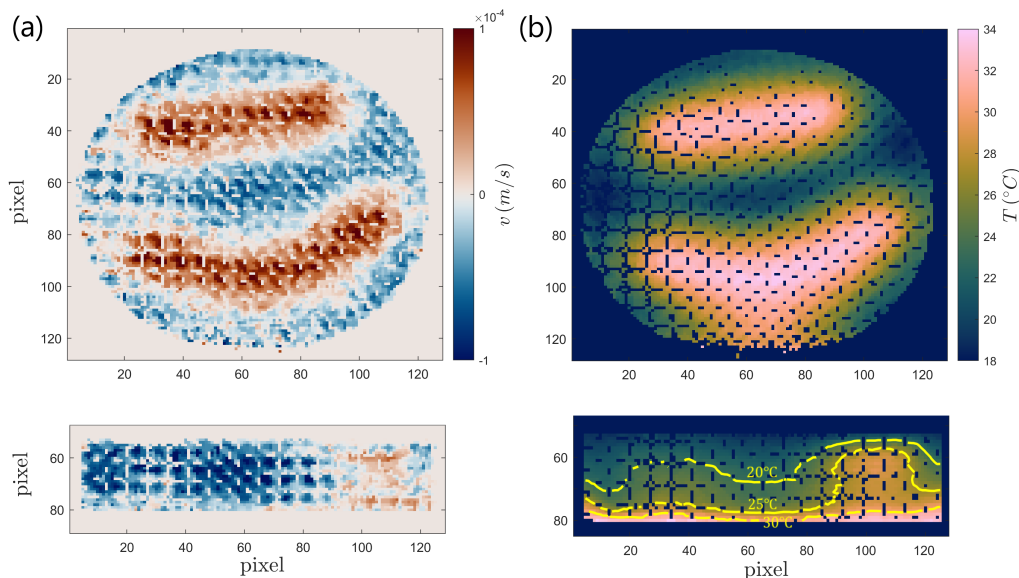


Figure 4: $\Delta T = 22.3^\circ\text{C}$, $Ra = 123.0$, $Da = 4.2 \times 10^{-4}$ and $Pr = 688.1$. (a) Vertical velocity field. (b) Temperature field. In the vertical cross-section of the temperature field we highlight the isotherms at 20°C , 25°C and 30°C .

341 our case. Moreover, from Fig. 4 it can be seen that the obtained macroscopic
 342 flow structure has a larger length scale than the pore scale. This represents
 343 one of the conditions needed for the flow to be described by the Darcy's
 344 law. The other is a negligible inertia term relative to viscous drag (Nield
 345 and Joseph, 1985). In our case, this can be estimated by evaluating the local
 346 Reynolds number Re^* based on the permeability of the medium, that is

$$Re^* = \frac{|\mathbf{v}| K^{0.5} \rho}{\eta}, \quad (3)$$

347 where $|\mathbf{v}|$ is the local velocity magnitude. For an inertia-free flow, Re^* must
 348 be small ($Re^* \ll 1$). This translates in terms of Rayleigh number as (Hewitt,
 349 2020):

$$\frac{Ra Da^{0.5}}{Pr} \ll 1. \quad (4)$$

350 The uncertainties for these non-dimensional numbers are discussed in Ap-
 351 pendix A.

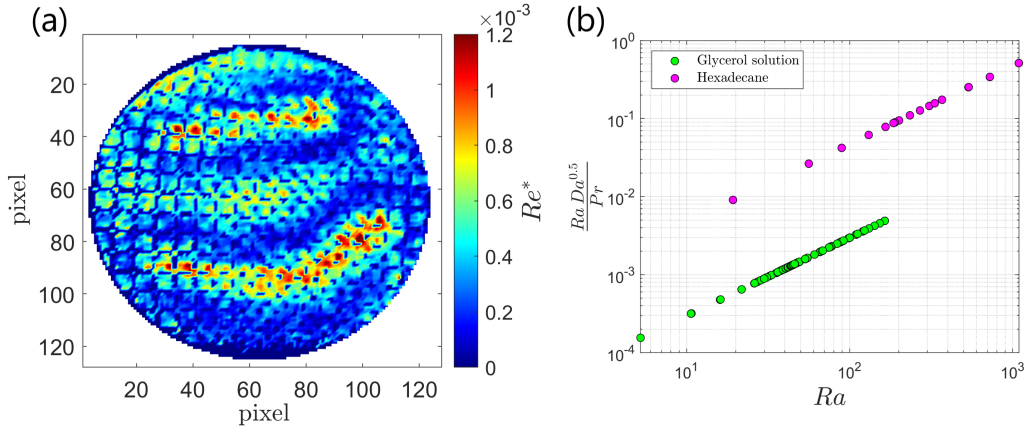


Figure 5: (a) Local Reynolds number Re^* for convection at $Ra = 131.2$, $Da = 4.2 \times 10^{-4}$ and $Pr = 688.1$. (b) Conditions needed for the flow to be described by the Darcy's law as a function of Ra for all our experiments.

352 Fig. 5a shows an example of Re^* calculated from the velocity field obtained
 353 from MRV for $Ra = 131.2$. In this case, Re^* remains much smaller
 354 than 1, which indicates that, under these conditions, the flow is inertia-free
 355 and can be described by the Darcy's law. Even considering the relatively
 356 large pores and the large porosity of our sample foam, this is valid for the
 357 majority of the experiments presented here. Only few experiments conducted
 358 with hexadecane are near the limit set by eq. (4), see Fig. 5b. In the follow-
 359 ing, the latter are used for qualitative purposes only.

360 Given the good correspondence between temperature field and velocity
 361 field at the same ΔT , we estimate the critical difference of temperature (ΔT_c)
 362 above which convection occurs directly from the temperature maps in the
 363 horizontal xy -plane. In fact, under our experimental conditions, temperature
 364 variations near the onset are better resolved than velocities, since the latter
 365 have very low values.

366 For the case where the fluid is the aqueous solution of glycerol, ΔT_c
 367 is found by evaluating the variance σ^2 of the images acquired at different Ra .
 368 This procedure is similar to that used by Hébert et al. (2010) to detect the
 369 onset of convection in the classical Rayleigh-Bénard configuration using the
 370 shadowgraph method. In our case, to achieve higher accuracy, the variance
 371 is computed within a squared region of length 50 ± 6 mm at the center of the

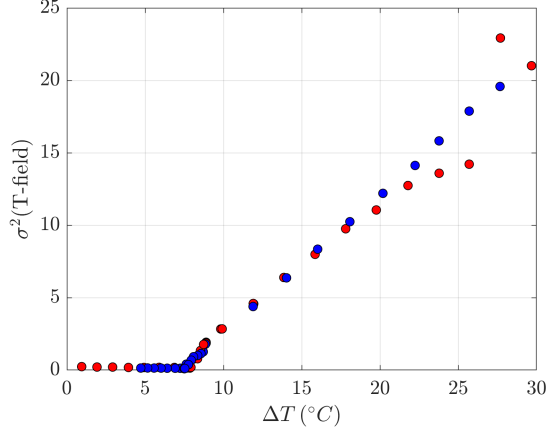


Figure 6: Variance σ^2 of the temperature field acquired on the xy -plane as a function of the imposed ΔT . The fluid is the glycerol aqueous solution. Blue symbols refer to decreasing ΔT , while red symbols refer to increasing ΔT .

372 temperature image obtained on the xy -plane.

373 The variance of the horizontal temperature field is plotted versus the
 374 imposed ΔT in Fig. 6. Red symbols refer to experiments conducted by
 375 increasing ΔT , and blue symbols to those conducted by decreasing ΔT . In
 376 both cases, the variance of the temperature field shows an abrupt increase
 377 at a specific critical value of ΔT . In the case of Fig. 6, this occurs at $\Delta T_c =$
 378 7.6 ± 0.1 °C. Below this temperature, σ^2 is stable around zero, indicating
 379 a very homogeneous and constant temperature field within the estimation
 380 area. This condition refers to the case where convection has not developed
 381 yet. For $\Delta T \geq \Delta T_c$, the variance of the temperature field increases with the
 382 imposed temperature difference. The jump of σ^2 between $\Delta T = 25.7$ °C and
 383 $\Delta T = 27.7$ °C (red symbols in Fig. 6) is caused by a change in the convection
 384 pattern. We will discuss this aspect in the next section. The value of ΔT_c
 385 and the fluid properties listed in Table 1 lead to a critical Rayleigh number of
 386 $Ra_c = 41.9$, with an uncertainty of $u(Ra_c) = 2.1$. The latter is in very good
 387 agreement with the theoretical value of $Ra_c = 4\pi^2$ expected for standard
 388 porous media.

389 4.2. Convection patterns

390 The convective pattern in terms of vertical velocity field for different
 391 Ra is shown in Fig. 7. Here the Rayleigh number is expressed as reduced

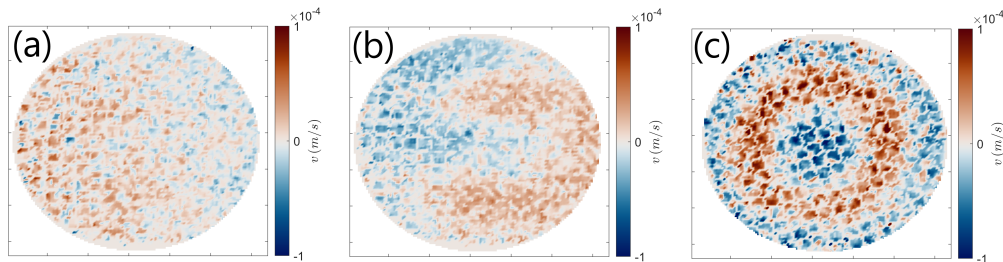


Figure 7: Convective pattern for different ϵ and $Pr = 688.1$. Here we show the vertical velocity fields for the xy -plane at $H/2$ obtained from MRV. (a) $\epsilon = -0.48$, (b) $\epsilon = 0.13$, (c) $\epsilon = 0.83$.

392 Rayleigh-Darcy number ϵ , that is

$$\epsilon = \frac{Ra - Ra_c}{Ra_c}. \quad (5)$$

393 In this case, ϵ was varied from -0.48 to 1.00 ($Pr = 688.1$). For $\epsilon = -0.48$
 394 (Fig. 7a), no motion is recognizable, the velocity always remains below the
 395 accuracy of the measurement, and the image shows only the magnitude of
 396 noise. Under similar conditions, Shattuck et al. (1997) show that convection
 397 can appear along side-walls if porosity increases locally due to structural
 398 defects in the porous medium or due to poor thermal insulation. This is
 399 not our case, where for $\epsilon < 0$ the onset of convection was never observed
 400 either in the bulk of the cavity or along its walls. This is also confirmed by
 401 MRT measures. As pointed out previously, at small Ra , MRT provides better
 402 visualizations than MRV because less noisy. The temperature fields obtained
 403 at $\epsilon < 0$ show an homogeneous and quasi-constant temperature in the regions
 404 of the image not affected by signal distortion during scan acquisition. This
 405 is shown in Fig. 8a by the normalized temperature profile T/\bar{T} along a
 406 cavity's diameter d (Fig. 8b), with \bar{T} being the mean temperature along d .
 407 For $\epsilon = -0.48$, T/\bar{T} remains relatively flat compared to cases with larger ϵ
 408 (Fig. 8a), especially toward the center of the cavity where the effect of signal
 409 distortion is minimal, indicating an homogeneous temperature field.

410 When ϵ is raised slightly above 0, convection is well established in the bulk
 411 of the fluid layer. For $\epsilon = 0.13$, two thick parallel rolls can be recognizable
 412 from both velocity (Fig. 7b) and temperature fields (Fig. 8b). Compared
 413 with the previous case, now the temperature profile across the convective pat-
 414 tern becomes more wavy, showing a clear increase in temperature variation

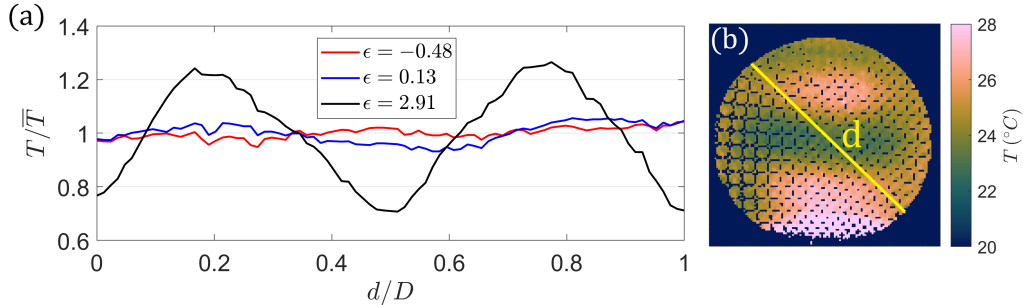


Figure 8: (a) Temperature profile along the cavity’s diagonal d (indicated in (b)) for $\epsilon = -0.48$, $\epsilon = 0.13$, and $\epsilon = 2.91$. The temperature is normalized by the mean temperature \bar{T} along d . d is normalized by the cavity diameter D . (b) Temperature fields at $\epsilon = 0.13$.

415 along d (Fig. 8b). The wavelength λ associated with the critical condition of
 416 motion can be estimated as the distance between the two rolls (e.g. distance
 417 between the local maxima of the temperature field). For $\epsilon = 0.13$ (Fig. 8b),
 418 we obtain a normalized wavelength λ/H of 2.04 ± 0.15 , leading to a critical
 419 wavenumber $\alpha_c = (2\pi H)/\lambda = (0.98 \pm 0.08)\pi$, very close to the value $\alpha_c = \pi$
 420 predicted by linear stability theory (Nield and Bejan, 2017).

421 In all the experiments we carried out, we found stable rolls up to $\epsilon = 5.43$,
 422 corresponding to $Ra = 270.2$. In this range of ϵ (i.e. $0 < \epsilon < 5.43$) the
 423 convective rolls organize themselves mainly as axisymmetric rolls (Fig. 7c),
 424 parallel rolls (Fig. 11a), or somewhere in between where one roll is slightly
 425 deformed and follows the shape of the container (Fig. 4). These different
 426 patterns developed in the same interval of ϵ are very likely due to variations
 427 of thermal boundary conditions at the sidewalls (Croquette et al., 1983).

428 In the case of axisymmetric rolls, the velocity field of Fig. 7c suggests
 429 the presence of small secondary convective structures perpendicular to the
 430 sidewall. To better display them, in Fig. 9a we plot only the positive verti-
 431 cal velocity obtained for $\epsilon = 0.64$. Here, between the main axisymmetric roll
 432 and the cavity’s sidewall, several narrow, elongated, upward-moving struc-
 433 tures surrounded by regions of down-welling are visible. Although images
 434 resolution does not allow us to evaluate their exact size and geometry, veloci-
 435 ties corresponding to these voxels are large enough to be quantified by MRV.
 436 This is done in Fig. 9b where the normalized positive vertical velocity is aver-
 437 aged along concentric circles with different radial coordinate r centered in
 438 the center of the image. It can be seen that the maximum positive average
 439 velocity is obtained at the axis of the main roll, while toward the central

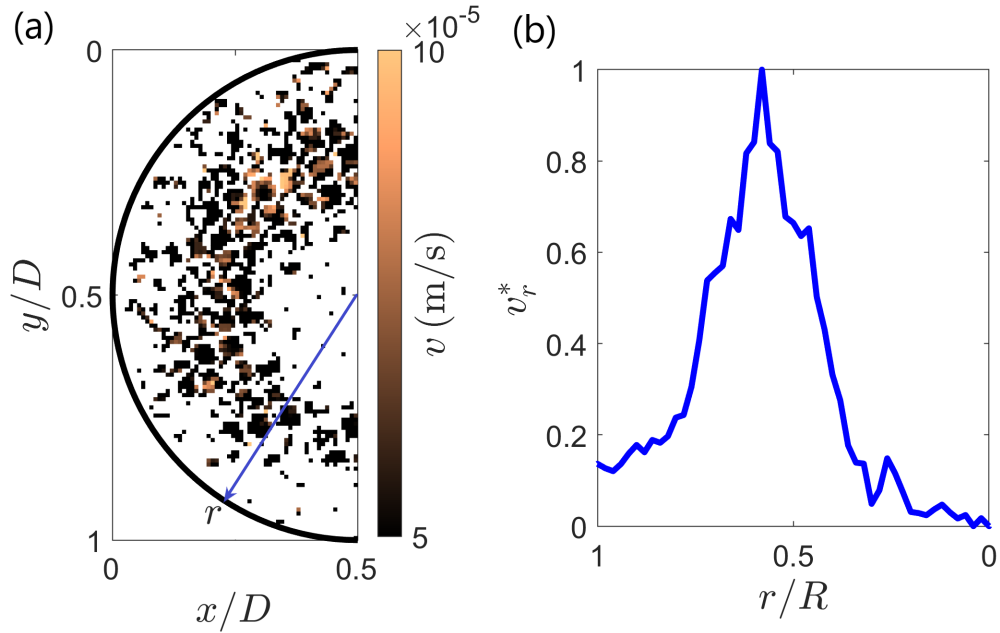


Figure 9: Axisymmetric convective pattern. (a) Positive vertical velocity image for half of the xy -plane. $\epsilon = 0.64$, $Pr = 688.1$. The thick black line delimits the wall of the cavity (with $R = D/2$ the cavity's radius). (b) Averaged positive vertical velocity normalized over its maximal value (v_r^*) along the radial direction.

440 region of the image, almost zero positive velocities are measured. On the
 441 other hand, in the region near the side wall, the presence of these upward-
 442 moving narrow rolls results in an average positive velocity larger than zero
 443 and equal to about 15 percent of the maximum average positive velocity.
 444 The same phenomena has been observed for classic Rayleigh-Bénard convec-
 445 tion. For instance, Croquette et al. (1983) observed unstable axisymmetric
 446 patterns characterized by the break down of the roll near to the sidewall
 447 to form a set of smaller rolls perpendicular to the cylindrical sidewall. In their
 448 case, the entire axisymmetric pattern later vanishes into a structure made of
 449 fairly regular rolls that always end perpendicular to the sidewalls. However,
 450 in our case the axisymmetric pattern remained stable throughout the entire
 451 duration of the experiment (up to a maximum of about 60 hours after the
 452 imposition of ΔT), during which the acquired images showed no changes in
 453 the convective pattern.

454 In Fig. 10 we show the main convective patterns obtained for another

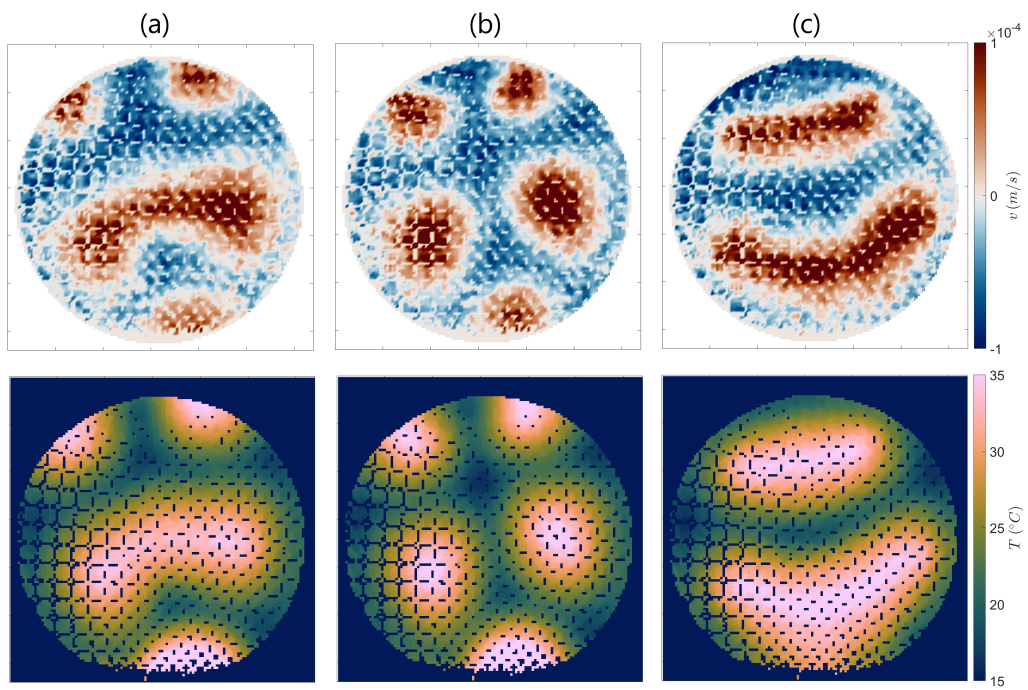


Figure 10: Different patterns for relatively small ϵ . The first row shows the vertical velocity images, while the second row shows the corresponding temperature field ($Pr = 688.1$). (a) $\epsilon = 2.38$, (b) $\epsilon = 2.64$, (c) $\epsilon = 2.91$.

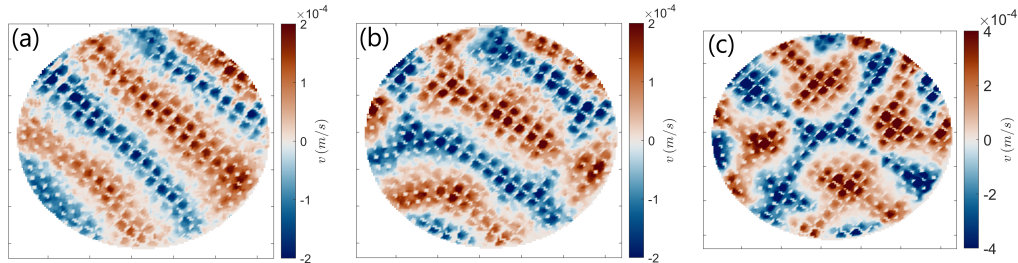


Figure 11: Convective pattern for hexadecane and different ϵ ($Pr = 43.5$). Here we show the vertical velocity fields for the xy -plane at $H/2$ obtained from MRV. (a) $\epsilon = 4.57$, (b) $\epsilon = 6.32$, (c) $\epsilon = 25.0$.

455 experiment where ϵ was varied from 0.82 to 2.91 ($Pr = 688.1$). In this case,
 456 images were obtained by increasing the previous temperature step by 2°C .
 457 From $\epsilon = 0.82$ to $\epsilon = 2.38$ we obtained the same pattern. In this case,
 458 both the velocity field and the temperature field show a warm up-rising roll
 459 at the center of the cavity and several warm plumes near the sidewall (Fig.
 460 10a). At the next temperature rise ($\epsilon = 2.64$), the central roll splits into two
 461 ends, resulting in polygonal cell pattern (Fig. 10b). Finally, at $\epsilon = 2.91$
 462 the different warm patches re-connect together to form two main rolls almost
 463 parallel each others (Fig. 10c). Interestingly, in this case the two rolls do
 464 not reach the sidewall, but no smaller structures are visible between them
 465 and the sidewall. The pattern change from Fig. 10b to Fig. 10c results in a
 466 sudden change in the variance of the temperature field in the xy -plane. This
 467 corresponds to the jump of σ^2 shown in Fig. 6 (red symbols).

468 The pattern evolution described above was not obtained when ϵ was de-
 469 creased from $\epsilon = 2.91$ to $\epsilon = 0.05$. When ϵ was decreased, the pattern
 470 obtained at the highest ϵ (i.e. the rolls in Fig. 10c) remained stable until ΔT
 471 was reduced to ΔT_c . This hysteresis in pattern evolution may be related to
 472 non-Boussinesq effects. These specific experiments were indeed carried out
 473 with glycerol solution as the saturating fluid, and the applied temperature
 474 difference corresponding to the polygonal cell pattern observed while increas-
 475 ing ΔT (Fig. 10b) was $\Delta T = 27.7^\circ\text{C}$. A similar hysteresis, in which both
 476 rolls and hexagonal convection pattern can be stable at the same Ra , takes
 477 place in Rayleigh-Bénard convection when the temperature dependence of
 478 fluid properties, such as thermal expansion coefficient and viscosity, is suf-
 479 ficiently large to result in up-down asymmetric conditions in the fluid layer
 480 (Busse, 1967; Darbouli et al., 2016).

481 Beside axisymmetric and deformed rolls, from $\epsilon = 2.95$ we observed also
482 stable parallel straight rolls. An example of them is shown in the velocity
483 field of Fig. 11a for hexadecane ($Pr = 43.5$, $\epsilon = 4.57$). In this case, the
484 wavenumber is $\alpha = (1.14 \pm 0.10)\pi$, slightly larger than α_c . This is in agree-
485 ment with the conditions for stable two-dimensional parallel rolls predicted
486 by theory (Joseph, 1976). In this case, rolls remained stable until $\epsilon \approx 6.32$,
487 corresponding to $Ra \approx 308.0$ and $\Delta T = 1.68$ °C. After that, rolls begin to
488 deform leading to a transitional regime (Fig. 11b). The Ra we obtained for
489 the beginning of this transition matches that predicted by numerical simu-
490 lations for the transition from a stationary convection regime to a periodic
491 regime characterized by the superposition of counter-rotating rolls. This
492 latter transition, that takes place for Ra in between 300 and 390 (Kimura
493 et al., 1987; Caltagirone and Fabrie, 1989), marks the beginning of thermal
494 boundary-layer instabilities that perturb (without completely destabilize) the
495 underlying convective structure (Hewitt, 2020). When ϵ is increased further,
496 we finally achieved a clearer cross-roll pattern (Fig. 11c).

497 4.3. Intensity of convection

498 The intensity of convection for $Ra > Ra_c$ can be evaluated from the
499 velocity image by calculating the squared mean large-scale flow velocity (U^2)
500 since $U^2 \sim E_K$, with E_K being the kinetic energy. The large-scale velocity is
501 defined as the surface integral of the magnitude of the velocity field \mathbf{v} , that
502 is

$$U^2 = \int_s \|\mathbf{v}\|^2 ds, \quad (6)$$

503 where s is the area of the velocity image on the xz -plane. In our case, U^2 is
504 calculated as the sum of the square of the velocity components for each pixel
505 of the velocity image.

506 Fig. 12 shows the large-scale velocity as a function of Ra . Here U is
507 normalized by the characteristic thermal diffusion velocity, κ_{eff}/H (with H
508 being the height of the cavity and κ_{eff} the effective thermal diffusivity). For
509 $Ra_c < Ra < 70$, a correlation between U and Ra is hard to identify because
510 data are very scattered. This is due to both the difficulty of distinguishing
511 low velocities from background noise and the underestimation of velocity
512 due to the accuracy limit of the MRV. For $Ra > 70$, Fig. 12 shows that
513 the normalized bulk velocity scales with Ra as $U \sim Ra^{1/2}$. This is the same
514 scaling obtained by weakly-nonlinear theory for classical Rayleigh-Bénard

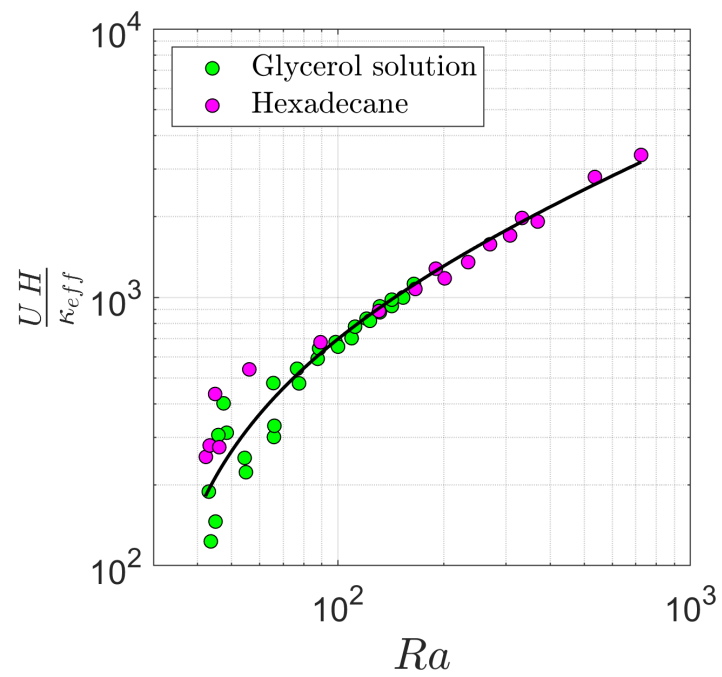


Figure 12: Normalized mean large-scale velocity U as a function of Ra . The solid line is the equation $y(x) = ax^{1/2} + b$, with $a = 147.3$ and $b = -774.4$.

515 convection at relatively small Ra (Schlüter et al., 1965), and for convection
 516 at low Re in porous media made by packed beds of spheres (Palm et al.,
 517 1972).

518 4.4. Heat transport

519 An aspect of interest in fluid-saturated porous media heated from below
 520 is to define the degree to which heat transfer is increased by convection.
 521 This can be captured by plotting the Nusselt number (Nu), namely the ratio
 522 between the total heat transferred in the system and the heat transferred by
 523 conduction alone at the same temperature difference, as a function of ϵ . For
 524 $\epsilon < 0$, heat is only transferred by conduction and $Nu = 1$. On the other
 525 hand, when convection starts ($\epsilon \geq 0$), the total heat transferred consists of
 526 a part due to conduction and a part due to convection leading to $Nu > 1$.

527 In our experiments with glycerol, Nu can be evaluated from the tempera-
 528 ture field obtained by MRT. To do so we used either the vertical cross-section
 529 in the xz -plane or the one along yz -plane, depending on the orientation of
 530 the convection pattern of each single experiment. In fact, some experiments
 531 are characterized by rolls parallel to one of the acquisition planes, limiting
 532 their use for evaluating heat transfer. To evaluate Nu we used only those
 533 images where at least one convective cell was well-resolved.

534 Fig. 13 shows an example of the local Nusselt number obtained for $\epsilon =$
 535 0.62. The local Nu is calculated as

$$Nu = \frac{-\lambda_{\text{eff}} \frac{\partial T}{\partial z}}{-\lambda_{\text{eff}} \frac{\Delta T}{H}}, \quad (7)$$

536 where the term $-\lambda_{\text{eff}}(\partial T/\partial z)$ is the total thermal flux, the term $-\lambda_{\text{eff}}(\Delta T/H)$
 537 is the conductive flux through the sample cavity, and λ_{eff} is the effective ther-
 538 mal conductivity of the system. The total thermal flux is obtained from our
 539 experiments by evaluating $\partial T/\partial z$ on the first three pixels from the bottom
 540 surface of the acquired images. Fig. 13a shows an example of the temperature
 541 field on the xz -plane used to calculate Nu . Here the convective rolls form two
 542 well-defined ascending warm regions surrounded by descending cold regions.
 543 The local Nu (Fig. 13b) calculated for each pixel-column of the temperature
 544 image follows this latter trend. Nu takes on relatively higher local values in
 545 colder regions, while decreasing as it approaches the warmer regions, with
 546 a minimum around the central axes of the latter. The slightly noisy trend
 547 for Nu is mainly due to the noise on the temperature field, especially in the

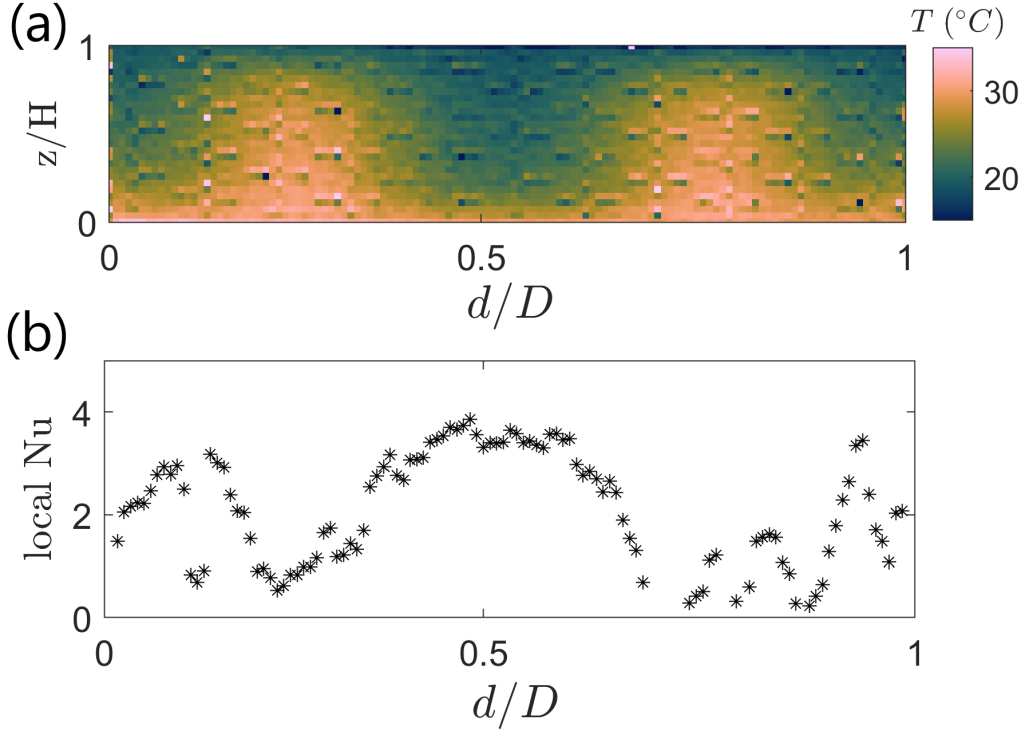


Figure 13: $Pr=688.1$, $\epsilon = 0.62$ and $\Delta T = 13.3$ °C. (a) Measured temperature field on the xz -plane during convection. (b) Variation of the local Nusselt number along the normalized cavity's diameter d/D .

548 first pixels near the bottom boundary. Given the resolution used to acquire
 549 these images, the interface between the cavity's bottom surface and the fluid
 550 above it is not always well resolved and may lead to some variation in the
 551 calculated local Nu .

552 From Fig. 13b one can evaluate the average Nusselt (\overline{Nu}) for a given ϵ
 553 as

$$\overline{Nu} = \frac{1}{\Sigma} \int_{\Sigma} Nu d\Sigma, \quad (8)$$

554 with Σ being the cavity's surface. The standard uncertainty is evaluated in
 555 $u_a(\overline{Nu}) = 0.1$. For the case in Fig. 13 we obtained $\overline{Nu} = 2.1$. Fig. 14
 556 reports the average Nusselt as a function of ϵ for all the experiments carried
 557 out using glycerol as saturating fluid. As expected, we recovered $\overline{Nu} = 1$ for

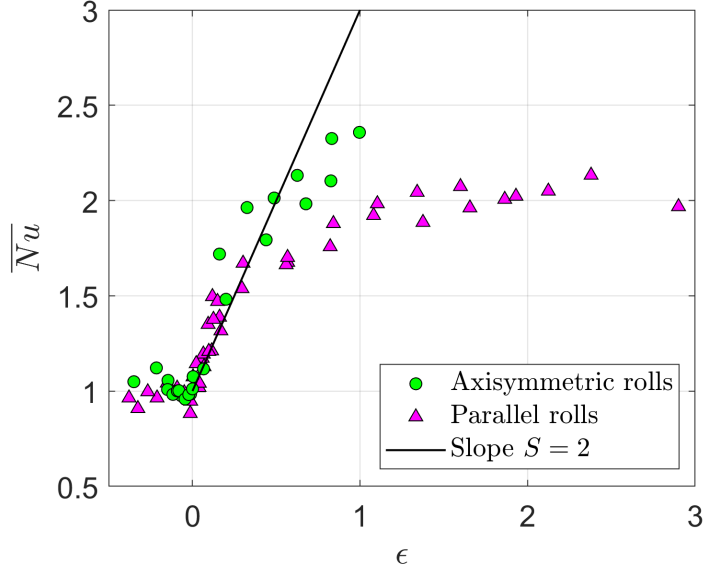


Figure 14: Average \overline{Nu} as a function of ϵ ($Pr = 688.1$). The different symbols represent the planes on which temperature images were acquired. The solid line shows a slope $S = 2$.

558 subcritical conditions and a sharp transition at the onset of bulk convection.
 559 For $\epsilon > 0$, \overline{Nu} increases linearly until about $\epsilon = 0.5$ where the slope begins
 560 to decrease until it saturates. The difference between the symbols in Fig.
 561 14 reflects the different acquisition planes used to estimate Nu . We used
 562 images along the xz -plane for experiments developing axisymmetric rolls,
 563 and images along the yz -plane for parallel rolls that are perpendicular to the
 564 image plane. Results for the axisymmetric case are the most reliable. This
 565 is due to the small signal distortion near the sidewall on the xz -plane and
 566 the fact that the local Nu can be easily integrated on the cavity's surface Σ
 567 given the axisymmetric conditions. On the other hand, to avoid the higher
 568 lateral distortion, for images of parallel rolls only a portion corresponding to
 569 one wavelength of the temperature field on the yz -plane was used. Together
 570 with the fact that the convective pattern is not axisymmetric, in this case
 571 the local Nu cannot be integrated over the entire surface of the cavity but
 572 only along the direction of the profile (\overline{Nu}_y). This leads to values of \overline{Nu}_y
 573 for parallel rolls that can only reflect an approximation of the real \overline{Nu} .

574 For both parallel and axisymmetric rolls, the results we obtained for the

575 $\overline{Nu}-\epsilon$ correlation in the interval $0 < \epsilon < 0.5$ show a linear trend with a
 576 slope $S = d\overline{Nu}/d\epsilon = 2$ (Fig. 14). The same slope is maintained for $\epsilon >$
 577 0.5 in the case of axisymmetric rolls. This is in agreement with the slope
 578 $S = 2$ predicted theoretically by Joseph (1976) for an unbounded porous
 579 layer (aspect ratio $\Gamma \rightarrow \infty$) with $Pr Da^{-1} \rightarrow \infty$. We recall that the aspect
 580 ratio in our case is $\Gamma = 4.4$ and $Pr Da^{-1} = 1.6 \times 10^6$ for glycerol and
 581 $Pr Da^{-1} = 1.0 \times 10^5$ for hexadecane.

582 Because of the accessibility of heat transfer measurements in experiments,
 583 this slope has been investigated experimentally in the past for several differ-
 584 ent systems. For a creeping flow through packed beds of spheres, Elder (1967)
 585 found a slope of $S = 1$, and Shattuck et al. (1997) found $S = 0.73 \pm 0.05$ for
 586 aspect ratios $\Gamma = 8 - 9$. Similar slopes were found by Howle et al. (1997),
 587 who obtained $0.53 < S < 1.35$ depending on the type of porous medium
 588 employed. Again with beads, Close et al. (1985) found that S is affected by
 589 the aspect ratio of the system, with a decrease in Γ leading to an increase
 590 in S . Beside porous media made by packed spheres, the $\overline{Nu}-\epsilon$ curve for a
 591 fluid-saturated highly porous metal foam was investigated by Kathare et al.
 592 (2008) and Davidson et al. (2009). For $\epsilon > 0$, the value of S they obtained
 593 is smaller than what we obtained in our system. This difference may be
 594 related to the different geometry and/or different thermal properties of the
 595 solid foam. That is, to the different viscous drag between a foam with regular
 596 structure and large pores (such as the one used in our experiments) and one
 597 with random structure and smaller pores. Or to the departure from the local
 598 thermal equilibrium between solid matrix and saturating fluid in the case of
 599 a highly conductive metal foam.

600 5. Conclusion

601 In this work, we carried out experiments of thermal convection at low-to-
 602 moderate Ra in a fluid-saturated solid foam heated from below and cooled
 603 from above. The solid foam consists of a 3D-printed open-cell structured
 604 plastic matrix with a porosity of $\phi = 0.83$ and four unit cells stacked on top
 605 of each other. Experimental investigations involving thermal convection in
 606 these types of porous media are essential because of their wide use in many
 607 heat and mass transfer applications, such as in latent heat thermal energy
 608 storage systems.

609 Natural convection in our system was studied using Magnetic Resonance
 610 Imaging (MRI). This technique allowed us to provide for the first time quan-

611 titative measurements of velocity vectors and temperature fields in the con-
612 vecting fluid. The results obtained were compared with those for classical
613 porous media (e.g. packed beds of spheres with $\phi < 0.5$) and with theoretical
614 predictions.

615 For our system, we first evaluated the relative importance of the inertia
616 term to the viscous resistance during convection. Even considering the large
617 porous size and high porosity of the foam, for the range of Ra over which the
618 experiments were performed, we obtained $Re^* < 1$ and thus an inertia-free
619 flow that can be effectively described by Darcy's law.

620 Next, we investigated the critical conditions of motion and the different
621 convection patterns. We found the onset of convection at $Ra_c = 41.9$, with
622 a critical wavenumber of $\alpha_c \approx \pi$, very close to the value predicted by linear
623 stability theory for Rayleigh-Darcy configuration. For $Ra < Ra_c$, we never
624 observed convection. In this case, the velocities always remain below the
625 accuracy of the measurement and temperature fields remain homogeneous
626 and constant. For $Ra_c \leq Ra < 308$, the flow organizes in stable rolls,
627 the latter in forms of axisymmetric, straight or deformed rolls. At about
628 $Ra = 308$, the flow enters in a transitional regime in which the convective
629 rolls begin to deform. At the highest Ra tested, the convective pattern
630 takes the form of well-developed cross-rolls. The intensity of convection
631 was estimated through the large-scale mean squared velocity U^2 , since $U^2 \sim E_K$,
632 with E_K as the kinetic energy of the system. For $Ra > 70$, we obtained
633 $U \sim Ra^{\frac{1}{2}}$, as it is for classic Rayleigh-Bénard convection without the porous
634 layer.

635 Finally, we estimated the Nusselt number from temperature fields. The
636 local Nu reflects the temperature distribution: higher values of local Nu cor-
637 respond to cold down-welling regions, and smaller Nu to warm up-welling
638 regions. The averaged Nusselt number for the whole system (\overline{Nu}) was esti-
639 mated from the local Nu of images with axisymmetric convective rolls and
640 parallel rolls. We obtained $\overline{Nu} = 1$ for subcritical conditions and a sharp
641 transition at the onset of convection. For experiments with axisymmetrical
642 rolls, when convection begins, \overline{Nu} increases as ϵ increases with a linear trend
643 with a slope $S = 2$. This is in agreement with the slope predicted by theory,
644 but is different from the slopes obtained in other experiments using different
645 systems. The differences with other experiments reported in the literature
646 may be associated with the different viscous drag that different porous ma-
647 trices can generate, the departure from local thermal equilibrium if the solid
648 and liquid components have very different thermal properties, and/or the

649 non-homogeneity of the porous medium.

650 **Appendix A.**

651 Uncertainties related to material properties measured in this work and
 652 those related to MRI techniques are reported in Sections 2.1 and 3.2, re-
 653 spectively. The uncertainty in the non-dimensional numbers is estimated by
 654 the error propagation method (Moffat, 1988). For a generic non-dimensional
 655 number R , this writes

$$u(R) = \sqrt{\sum_{i=1}^N \left(\frac{\partial R}{\partial X_i} u(X_i) \right)^2}, \quad (\text{A.1})$$

656 with R as a function of N independent variables (X_i), each with its own
 657 uncertainty $u(X_i)$. This leads, for instance, the uncertainty for the Prandtl
 658 number (defined as $Pr = \eta/(\rho\kappa_{\text{eff}})$) being

$$u(Pr) = \sqrt{\left(\frac{\partial Pr}{\partial \eta} u_a(\eta) \right)^2 + \left(\frac{\partial Pr}{\partial \rho} u_a(\rho) \right)^2 + \left(\frac{\partial Pr}{\partial \kappa_{\text{eff}}} u_a(\kappa_{\text{eff}}) \right)^2}, \quad (\text{A.2})$$

659 with $u_a(\eta) = 5 \times 10^{-4}$ Pa s, $u_a(\rho) = 0.01$ kg m⁻³, and $u_a(\kappa_{\text{eff}}) = 3.5 \times 10^{-9}$
 660 m²s⁻¹ (Sgreva et al., 2023). This results in $u(Pr) = 24.9$ for the glycerol-
 661 saturated foam and $u(Pr) = 7.4$ for hexadecane-saturated foam.

662 Uncertainties for the other non-dimensional numbers are obtained in the
 663 same way, i.e. according to eq. (A.1) and their definitions. For the Rayleigh
 664 number, we estimate $u(Ra_c) = 2.1$ at the onset of convective motion for the
 665 glycerol-saturated foam. For that we consider, in addition to the uncertain-
 666 ties given above, also $u_a(H) = 0.01$ mm, $u_a(\beta) = 2.6$ °C⁻¹ and $u_a(T) = 0.10$
 667 °C for the temperature at the upper and lower cavity's surfaces.

668 **Acknowledgments**

669 This work was funded by the operation STOCK'NRJ, co-financed by
 670 the European Regional Development Fund within the framework of the Pro-
 671 gram FEDER-FSE Lorraine and Massif des Vosges 2019–2023. This work is
 672 also part of the project CONVINCES, financially supported by the French
 673 National Research Agency (Grant No. ANR-21-CE50-0029).

674 **References**

- 675 Agyenim, F., Hewitt, N., Eames, P., Smyth, M., 2010. A review of materials,
676 heat transfer and phase change problem formulation for latent heat thermal
677 energy storage systems (LHTESS). *Renewable and Sustainable Energy*
678 *Reviews* 14, 615–628.
- 679 Ataei-Dadavi, I., Chakkingal, M., Kenjeres, S., Kleijn, C.R., Tummars, M.J.,
680 2019. Flow and heat transfer measurements in natural convection in coarse-
681 grained porous media. *International Journal of Heat and Mass Transfer*
682 130, 575–584.
- 683 Busse, F.H., 1967. The stability of finite amplitude cellular convection and
684 its relation to an extremum principle. *Journal of Fluid Mechanics* 30,
685 625–649.
- 686 Caltagirone, J., Fabrie, P., 1989. Natural convection in a porous medium at
687 high Rayleigh numbers. I: Darcy’s model. *European Journal of mechanics.*
688 *B, Fluids* 8, 207–227.
- 689 Close, D., Symons, J., White, R., 1985. Convective heat transfer in shallow,
690 gas-filled porous media: experimental investigation. *International Journal*
691 *of Heat and Mass Transfer* 28, 2371–2378.
- 692 Croquette, V., Mory, M., Schosseler, F., 1983. Rayleigh-bénard convective
693 structures in a cylindrical container. *Journal de Physique* 44, 293–301.
- 694 Darbouli, M., Métivier, C., Leclerc, S., Nouar, C., Bouteera, M., Stemme-
695 len, D., 2016. Natural convection in shear-thinning fluids: Experimental
696 investigations by MRI. *International Journal of Heat and Mass Transfer*
697 95, 742–754.
- 698 Davidson, J.H., Kulacki, F., Savela, D., 2009. Natural convection in water-
699 saturated reticulated vitreous carbon foam. *International Journal of Heat*
700 *and Mass Transfer* 52, 4479–4483.
- 701 Diersch, H.J., Kolditz, O., 2002. Variable-density flow and transport in
702 porous media: approaches and challenges. *Advances in Water Resources*
703 25, 899–944.
- 704 Dukhan, N., Minjeur, C.A., 2011. A two-permeability approach for assessing
705 flow properties in metal foam. *Journal of Porous Materials* 18, 417–424.

- 706 Elder, J.W., 1967. Steady free convection in a porous medium heated from
707 below. *Journal of Fluid Mechanics* 27, 29–48.
- 708 Gasow, S., Kuznetsov, A.V., Jin, Y., 2022. Prediction of pore-scale-property
709 dependent natural convection in porous media at high Rayleigh numbers.
710 *International Journal of Thermal Sciences* 179, 107635.
- 711 Hashin, Z., Shtrikman, S., 1962. A variational approach to the theory of
712 the effective magnetic permeability of multiphase materials. *Journal of*
713 *Applied Physics* 33, 3125–3131.
- 714 Hébert, F., Hufschmid, R., Scheel, J., Ahlers, G., 2010. Onset of rayleigh-
715 Bénard convection in cylindrical containers. *Physical Review E* 81, 046318.
- 716 Hennig, J., Nauerth, A., Friedburg, H., 1986. RARE imaging: a fast imaging
717 method for clinical MR. *Magnetic Resonance in Medicine* 3, 823–833.
- 718 Hewitt, D., 2020. Vigorous convection in porous media. *Proceedings of the*
719 *Royal Society A* 476, 20200111.
- 720 Horton, C., Rogers Jr, F., 1945. Convection currents in a porous medium.
721 *Journal of Applied Physics* 16, 367–370.
- 722 Howle, L., 2002. Convection in ordered and disordered porous layers, in:
723 *Transport Phenomena in Porous Media II*. Elsevier, pp. 155–176.
- 724 Howle, L., Behringer, R., Georgiadis, J., 1997. Convection and flow in porous
725 media. Part 2. Visualization by shadowgraph. *Journal of Fluid Mechanics*
726 332, 247–262.
- 727 Joseph, D.D., 1976. *Stability of fluid motions II*. Springer Berlin, Heidelberg.
- 728 Kathare, V., Davidson, J., Kulacki, F., 2008. Natural convection in water-
729 saturated metal foam. *International Journal of Heat and Mass Transfer*
730 51, 3794–3802.
- 731 Kimura, S., Schubert, G., Straus, J.M., 1987. Instabilities of steady, periodic,
732 and quasi-periodic modes of convection in porous media. *Journal of Heat*
733 *Transfer* 109, 350–355. doi:10.1115/1.3248087.

- 734 Klochko, L., Noel, J., Sgreva, N., Leclerc, S., Métivier, C., Lacroix, D.,
735 Isaiev, M., 2022. Thermophysical properties of n-hexadecane: Combined
736 molecular dynamics and experimental investigations. *International Com-*
737 *munications in Heat and Mass Transfer* 137, 106234.
- 738 Krishna, D.J., Basak, T., Das, S.K., 2009. Natural convection in a non-
739 darcy anisotropic porous cavity with a finite heat source at the bottom
740 wall. *International Journal of Thermal Sciences* 48, 1279–1293.
- 741 Kumar, P., Topin, F., 2017. State-of-the-art of pressure drop in open-cell
742 porous foams: review of experiments and correlations. *Journal of Fluids*
743 *Engineering* 139.
- 744 Lapwood, E., 1948. Convection of a fluid in a porous medium, in: *Math-*
745 *ematical Proceedings of the Cambridge Philosophical Society*, Cambridge
746 *University Press*. pp. 508–521.
- 747 Leclerc, S., Métivier, C., 2018. MRI temperature and velocity measurements
748 in a fluid layer with heat transfer. *Experiments in Fluids* 59, 1–9.
- 749 Moffat, R.J., 1988. Describing the uncertainties in experimental results.
750 *Experimental thermal and fluid science* 1, 3–17.
- 751 Nield, D., Joseph, D.D., 1985. Effects of quadratic drag on convection in a
752 saturated porous medium. *The Physics of Fluids* 28, 995–997.
- 753 Nield, D.A., Bejan, A., 2017. *Convection in porous media*. 5, Springer Cham.
- 754 Noel, J., Metivier, C., Becker, S., Leclerc, S., 2022. Natural convection in
755 phase change material: Experimental study. *International Journal of Heat*
756 *and Mass Transfer* 183, 122047.
- 757 Palm, E., Weber, J.E., Kvernfold, O., 1972. On steady convection in a
758 porous medium. *Journal of Fluid Mechanics* 54, 153–161.
- 759 Qureshi, Z.A., Elnajjar, E., Al-Ketan, O., Al-Rub, R.A., Al-Omari, S.B.,
760 2021. Heat transfer performance of a finned metal foam-phase change ma-
761 terial (FMF-PCM) system incorporating triply periodic minimal surfaces
762 (TPMS). *International Journal of Heat and Mass Transfer* 170, 121001.

- 763 Rees, D.A.S., Lage, J., 1996. The effect of thermal stratification on natural
764 convection in a vertical porous insulation layer. *International Journal of*
765 *Heat and Mass Transfer* 40, 111–121.
- 766 Schlüter, A., Lortz, D., Busse, F., 1965. On the stability of steady finite
767 amplitude convection. *Journal of Fluid Mechanics* 23, 129–144.
- 768 Sgreva, N.R., Jannot, Y., Métivier, C., 2023. Effective thermal diffusivity
769 and conductivity of a fluid-saturated solid foam. *Review of Scientific In-*
770 *struments* 94.
- 771 Sgreva, N.R., Noel, J., Metivier, C., Marchal, P., Chaynes, H., Isaiev, M.,
772 Jannot, Y., 2022. Thermo-physical characterization of hexadecane during
773 the solid/liquid phase change. *Thermochimica Acta* 710, 179180.
- 774 Shattuck, M., Behringer, R., Johnson, G., Georgiadis, J., 1995. Onset and
775 stability of convection in porous media: Visualization by magnetic reso-
776 nance imaging. *Physical review letters* 75, 1934.
- 777 Shattuck, M., Behringer, R., Johnson, G., Georgiadis, J.G., 1997. Convection
778 and flow in porous media. part 1. visualization by magnetic resonance
779 imaging. *Journal of Fluid Mechanics* 332, 215–245.
- 780 Shiina, Y., Hishida, M., 2010. Critical Rayleigh number of natural convection
781 in high porosity anisotropic horizontal porous layers. *International Journal*
782 *of Heat and Mass Transfer* 53, 1507–1513.
- 783 Skuntz, M.E., Perera, D., Maneval, J.E., Seymour, J.D., Anderson, R., 2018.
784 Melt-front propagation and velocity profiles in packed beds of phase-change
785 materials measured by magnetic resonance imaging. *Chemical Engineering*
786 *Science* 190, 164–172.
- 787 Skuntz, M.E., Seymour, J.D., Anderson, R., 2021. Observation of heat
788 transfer due to variable thermophysical properties of sub-, near-and super-
789 critical fluids in porous media by magnetic resonance imaging. *Interna-*
790 *tional Communications in Heat and Mass Transfer* 128, 105635.
- 791 Smith, D.S., Alzina, A., Bourret, J., Nait-Ali, B., Pennec, F., Tessier-Doyen,
792 N., Otsu, K., Matsubara, H., Elser, P., Gonzenbach, U.T., 2013. Thermal
793 conductivity of porous materials. *Journal of Materials Research* 28, 2260–
794 2272.

- 795 Tait, S., Jaupart, C., 1992. Compositional convection in a reactive crystalline
796 mush and melt differentiation. *Journal of Geophysical Research: Solid*
797 *Earth* 97, 6735–6756.
- 798 Takamura, K., Fischer, H., Morrow, N.R., 2012. Physical properties of aque-
799 ous glycerol solutions. *Journal of Petroleum Science and Engineering* 98,
800 50–60.
- 801 Wang, S., Cheng, Z., Jiang, L., Song, Y., Liu, Y., 2021. Quantitative study of
802 density-driven convection mass transfer in porous media by MRI. *Journal*
803 *of Hydrology* 594, 125941.
- 804 Weber, M., Kimmich, R., 2002. Rayleigh-bénard percolation transition of
805 thermal convection in porous media: Computational fluid dynamics, NMR
806 velocity mapping, NMR temperature mapping. *Physical Review E* 66,
807 056301.
- 808 Yang, H., Li, Y., Ma, B., Zhu, Y., 2021. Review and a theoretical approach on
809 pressure drop correlations of flow through open-cell metal foam. *Materials*
810 14, 3153.
- 811 Yao, Y., Wu, H., Liu, Z., Gao, Z., 2018. Pore-scale visualization and mea-
812 surement of paraffin melting in high porosity open-cell copper foam. *In-*
813 *ternational Journal of Thermal Sciences* 123, 73–85.
- 814 Zhang, S., Feng, D., Shi, L., Wang, L., Jin, Y., Tian, L., Li, Z., Wang, G.,
815 Zhao, L., Yan, Y., 2021. A review of phase change heat transfer in shape-
816 stabilized phase change materials (ss-PCMs) based on porous supports for
817 thermal energy storage. *Renewable and Sustainable Energy Reviews* 135,
818 110127.